ACS APPLIED MATERIALS & INTERFACES

Research Article

Cite This: *ACS Appl. Mater. Interfaces* 2019, 11, 37822−37832

www.acsami.org

Novel Au/La-Bi_5O_7I Microspheres with Efficient Visible-Light Photocatalytic Activity for NO Removal: Synergistic Effect of Au Nanoparticles, La Doping, and Oxygen Vacancy

Jingyu Zhang,[†,‡] Gangqiang Zhu,*[,†] Shiping Li,[†] Fei Rao,[†] Qadeer-Ul Hassan,[†] Jianzhi Gao,[†]
Yu Huang,*[,§] and Mirabbos Hojamberdiev[∥]

[†]School of Physics and Information Technology, Shaanxi Normal University, 710062 Xi'an, P. R. China

[‡]School of Materials Science and Engineering National Institute for Advanced Materials, Nankai University, 300350 Tianjin, P. R. China

[§]State Key Lab of Loess and Quaternary Geology (SKLLQG), Institute of Earth Environment, Chinese Academy of Sciences, 710061 Xi'an, P. R. China

[∥]Fachgebiet Keramische Werkstoffe, Institut für Werkstoffwissenschaften und -technologien, Technische Universität Berlin, Hardenbergstraße 40, 10623 Berlin, Germany

Supporting Information

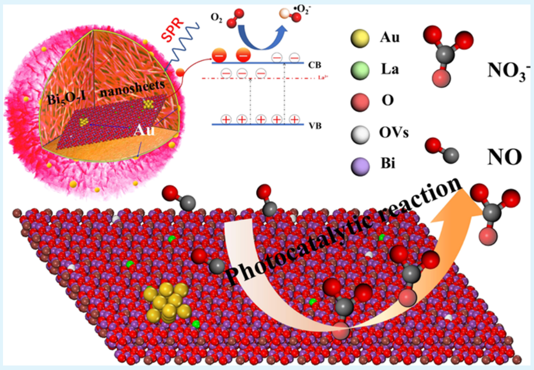

ABSTRACT: Sphere-like Bi_5O_7I (BOI) doped with La (L-BOI) samples were prepared by a solvothermal method followed by calcination at 450 °C for 2 h. Au nanoparticles were loaded on 6% La-doped Bi_5O_7I (2%A−6%L-BOI) microspheres by a room-temperature chemical reduction method. The UV−vis absorption spectra show that the L-BOI and 2%A−6%L-BOI samples have a strong visible-light absorption in comparison with the pure BOI. The electron paramagnetic resonance results indicate that the number of oxygen vacancies in L-BOI samples is increased with an increasing amount of the La dopant. The band structure of the prepared photocatalysts is investigated by confirming the positions of the valence band (VB) measured by XPS-VB and the Fermi level computed by density functional theory, respectively. NO is selected as a target gaseous pollutant to confirm the influence of La doping and the plasmonic effect of Au nanoparticles on the photocatalytic activity of BOI microspheres. The 2%A−6%L-BOI sample exhibits an enhanced photocatalytic performance compared to BOI, L-BOI, and A-BOI photocatalysts under visible-light irradiation. Interestingly, the 2%A−6%L-BOI sample also can reduce the amount of intermediate NO_2 during the NO removal process. The enhanced photocatalytic efficiency of the 2%A−6%L-BOI photocatalyst is profited from the synergy of La-ion doping, oxygen vacancy, and the surface plasmon resonance effect of Au nanoparticles. Based on the results of trapping experiments and electron spin resonance spectroscopy tests, h^+, e^-, and $^•O_2^-$ were involved in the NO oxidative removal.

KEYWORDS: *bismuth oxyhalide, Bi_5O_7I, lanthanum doping, Au nanoparticles, oxygen vacancy, NO_x removal*

1. INTRODUCTION

Photocatalysis is considered as one of the promising remediation techniques in environmental purification for water pollution and hazardous gases because of its economic feasibility, nontoxicity, resource-saving, and environment-friendliness.[1,2] Therefore, it is indispensable to develop efficient and stable semiconductor-based photocatalysts. The light utilization and separation of charge carriers in photocatalysts are two key factors determining the overall photocatalytic efficiency.[3,4] In order to efficiently enhance the utilization of solar energy and separation of charge carriers, extensive efforts have been made to study the optimization for innovative photocatalysts in the last 40 years.[5−7]

Recently, novel photocatalysts have been developed by cation/anion doping,[8] constructing of semiconductor/semiconductor heterojunctions,[9] and surface modification with noble metal nanoparticles and quantum dots.[10] Particularly, doping a semiconductor with transition metals has attracted much attention because of its several merits. First, the induction of a bathochromic shift, that is, narrowing the wide band gap by introducing the intraband gap states, is done to enhance its visible-light response.[11] Second, doping with metal ions having variable valency (Cr^{3+}, Mn^{3+}, Cu^{2+}, Fe^{3+},

Received: August 10, 2019
Accepted: September 24, 2019
Published: September 24, 2019

DOI: 10.1021/acsami.9b14300
ACS Appl. Mater. Interfaces 2019, 11, 37822−37832

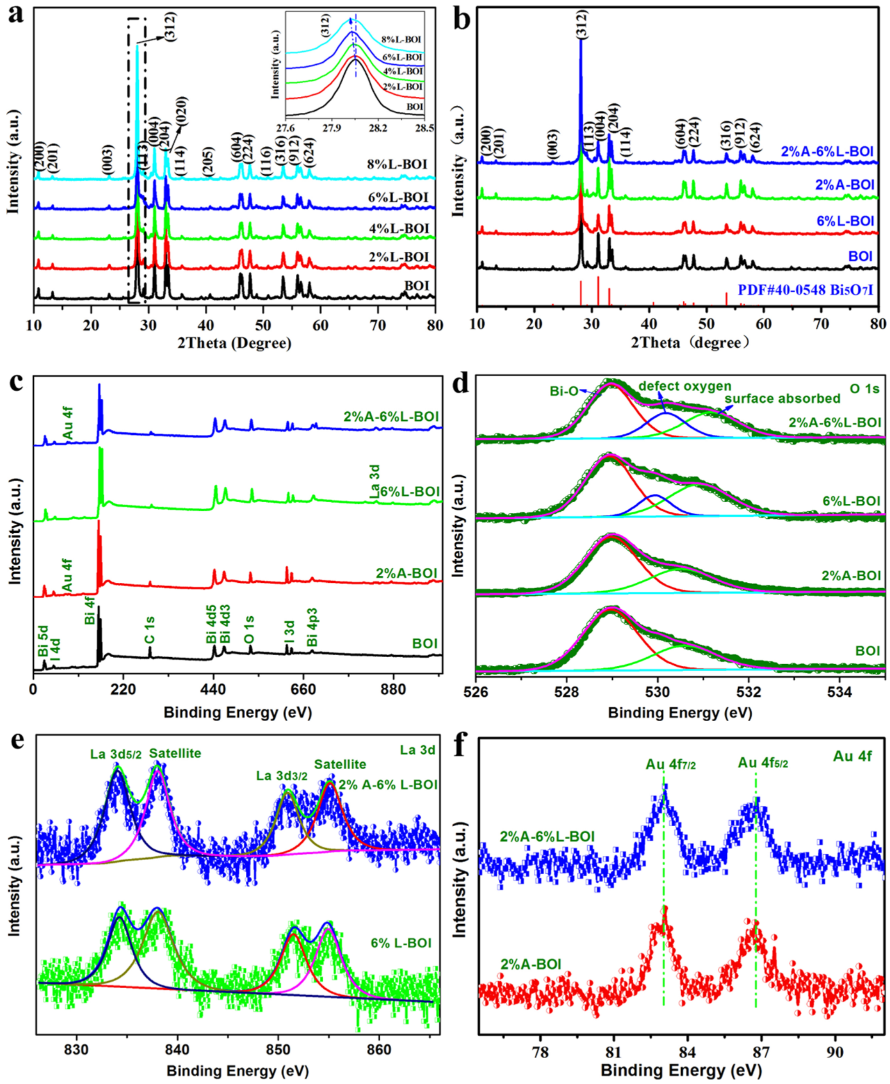

Figure 1. XRD patterns of La-doped BOI samples (a), an enlarged view of the main diffraction (312) peak (inset); XRD patterns of BOI, 2%A-BOI, 6%L-BOI and 2%A–6%L-BOI samples (b); XPS survey spectra (c), O 1s (d), La 3d (e) and Au 4f (f) high-resolution XPS spectra of the prepared samples.

etc.) are beneficial to trap electrons and holes, which further prevents the recombination of photogenerated e^- and h^+ pairs.[12,13] Specifically, doping with lanthanide ions also can obviously improve photocatalytic efficiency by the virtue of the following two factors. First, the lanthanide ions can trap photogenerated electrons as efficient scavengers, raising the separation efficiency of the photo-excited charge carriers.[14−17] Second, the doped lanthanide ions with large radius can induce lattice defects, which leads to the formation of oxygen vacancies, improving the photocatalytic activity.[18,19] For instance, Atikur and Jayaganthan.[18] found that La^{3+} and Dy^{3+} co-doped ZnO nanoparticles possess excellent photocatalytic active for the degradation of methylene blue dye than the pure ZnO particles under visible-light irradiation. La^{3+} and Dy^{3+} can be incorporated into the ZnO lattice to improve the light absorption and to form oxygen vacancy, resulting in efficient light utilization and high separation efficiency of charge carriers.

Bismuth-rich oxyiodides ($Bi_xO_yI_z$), including BiOI,[20] $Bi_4O_5I_2$,[21] $Bi_7O_9I_3$,[22] and Bi_5O_7I,[8,23] have been reported to possess promising applications as efficient photocatalysts for the removal of pollutants because of their special layered structures. The layered structures are favorable for the separation of photo-induced charge carriers by an internal electric field.[24,25] Furthermore, with the increasing Bi/I ratio, the value of band gap changes from 1.80 to 2.90 eV.[26−29] Especially, Bi_5O_7I exhibited excellent photocatalytic performance for organic pollutants degradation and N_2 fixation owing to its negatively positioned conduction band (CB).[28,29] Unfortunately, the band gap of Bi_5O_7I is about 2.90 eV,[8,30] resulting in a weak visible-light response. Therefore, it is necessary to modulate its electronic band structures with an enhanced visible-light response.

In this study, we attempt to synthesize La-doped Bi_5O_7I microspheres by a solvothermal method followed by calcination. It is expected that the oxygen vacancies in La-doped Bi_5O_7I will narrow down the band gap. Moreover, Au nanoparticles loaded on La-Bi_5O_7I microspheres have visible-light absorption characteristics because of the surface plasmon resonance (SPR) effect. The electronic band structures of the synthesized photocatalysts were investigated by theoretical calculations and experimental measurements. The photocatalytic performances of the prepared samples for NO oxidative removal were investigated. The mechanisms of

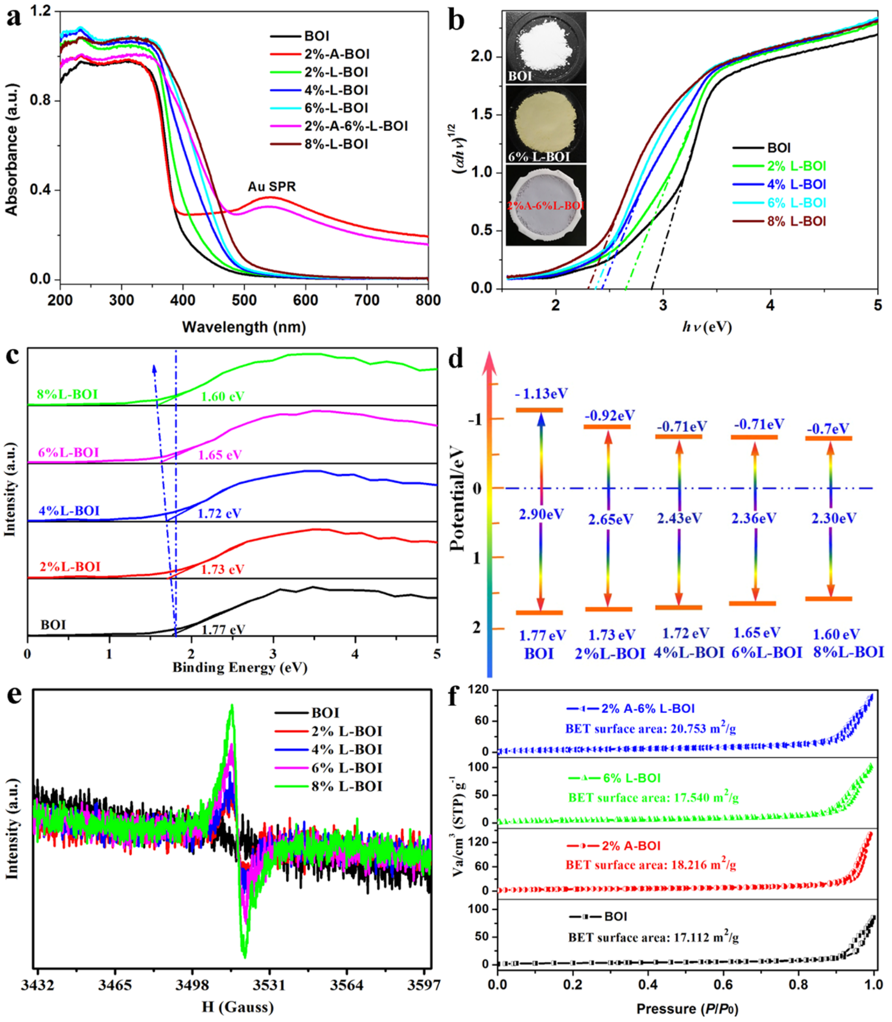

Figure 2. UV−vis absorption spectra (a) and Tauc plots of $(\alpha h\nu)^{1/2}$ vs photon energy $h\nu$ (b) of the prepared samples (inset photographs indicate the colors of BOI, 6%L-BOI and 2%A−6%L-BOI powders); valence-band XPS spectra (c), band structures (d), EPR spectra (e) and N_2 adsorption−desorption isotherms of the prepared samples (f).

enhanced photocatalytic activity for NO removal by the Au nanoparticle-loaded La-doped Bi_5O_7I microspheres photocatalysts are also discussed in this study.

2. EXPERIMENTAL SECTION

2.1. Synthesis. All chemicals obtained from ALADDIN Reagent Co., Ltd. were of analytical grade and used without further purification. The synthesis procedure of porous BiOI microspheres is given in detail in the Supporting Information.[30] La-doped BiOI was synthesized by applying an identical synthesis procedure of BiOI with the addition of $La(NO)_3 \cdot 6H_2O$ into the solution in a varying content (2, 4, 6, and 8 mol %). Bi_5O_7I (BOI) and La-doped Bi_5O_7I (L-BOI) samples were synthesized by calcining precursor BiOI and La-doped BiOI samples at 450 °C for 2 h.[30] 2 wt % Au nanoparticles were deposited on the BOI and 6 mol % La-doped BOI samples by a room-temperature chemical reduction method. In a typical procedure, 50 mg of BOI or 6 mol % La-doped BOI was dispersed in 100 mL of absolute ethanol, and 1 mg of $HAuCl_4$ was introduced into the suspension. Then, 3 mL of 0.04 M $C_6H_5Na_3O_7$ solution was added into the suspension and with continuous stirring for 30 min, resulting in a lavender precipitate. Finally, the prepared samples were collected and cleaned. Hereafter, 2 wt % Au-deposited BOI, 6 mol % La-doped BOI, and 2 wt % Au-deposited 6 mol % La-doped BOI are labeled as 2%A-BOI, 6%L-BOI, and 2%A−6%L-BOI, respectively.

2.2. Characterization. The crystal phase structures and morphologies of the prepared photocatalysts were analyzed by means of X-ray diffractometer (XRD, D/max-2550, Rigaku), scanning electron microscopy (SEM, Nova NanoSEM 450, FEI), and transmission electron microscopy (TEM, JEM-2100, JEOL), respectively. The electron paramagnetic resonance (EPR) and electron spin resonance (ESR) spectra were recorded on an ER200-SRC (Bruker) at room temperature. X-ray photoelectron spectroscopy (XPS) analysis was carried out on an ESCALAB MKII X-ray photoelectron spectrometer (VG Scientific). The ultraviolet−visible absorption spectra were recorded on a (Cary 5000, Agilent) UV−visible spectroscope with a wavelength range of 200−800 nm.

2.3. Photocatalytic Activity Test. The photo-oxidation process of NO over the prepared samples was studied by in situ Fourier-transform infrared spectroscopy (FTIR) in a closed flow reactor. A more detailed procedure of photocatalytic removal of NO and in situ FTIR are given in the Supporting Information.

3. RESULTS AND DISCUSSION

3.1. Characterization of the Prepared Photocatalysts.

Figure 1a shows the XRD patterns of the as-synthesized pure BOI and L-BOI samples. It is obvious that the diffraction peaks of the pure BOI are in good agreement with the orthorhombic Bi_5O_7I (ICDD PDF# 40-0548). Despite an increase in the content of La^{3+} up to 8 mol %, a pure phase without any secondary phase was formed. An obvious shift in the diffraction peak of (312) is noted in the XRD patterns of La^{3+}-doped BOI

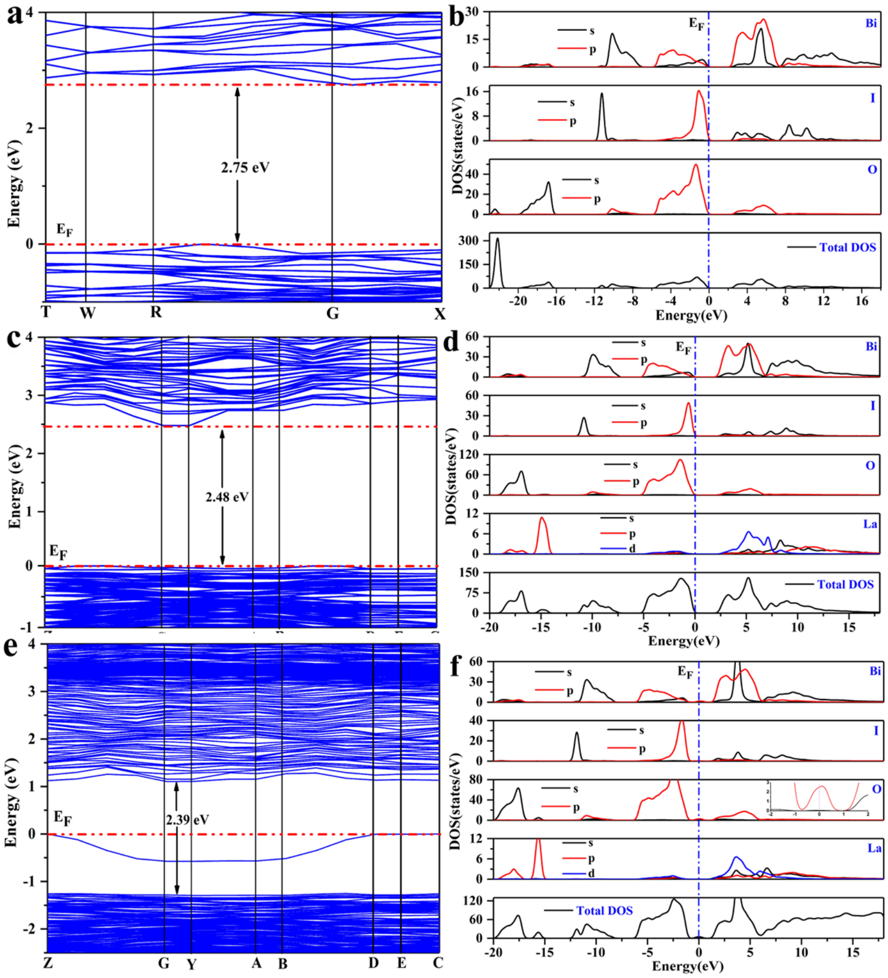

Figure 3. Band structures and PDOS/TDOS of pure BOI (a,b), La-doped BOI (c,d), and La-doped BOI with oxygen defects (e,f).

samples (Figure 1a) because of the larger ionic radius of La^{3+} (0.188 nm) than that of Bi^{3+} (0.103 nm),[15] indicating that La^{3+} was successfully introduced into the BOI crystal lattice.[19,31,32] Moreover, the introduction of Au nanoparticles has an insignificant effect on the BOI crystal structure (Figure 1b).

To further investigate the chemical composition and oxidation states of the elements on the surface of the photocatalysts, the pure BOI, 6%L-BOI, 2%A-BOI, and 2% A−6%L-BOI samples were analyzed by XPS (Figure 1c−f). In Figure 1c, the signals of Bi, O, and I elements were detected in the pure BOI, 6%L-BOI, 2%A-BOI, and 2%A−6%L-BOI samples. La was observed in 2%L-BOI and 2%A−6%L-BOI samples, whereas Au was present in 2%A-BOI and 2%A−6%L-BOI samples. As shown, the signals of the La and Au are much weaker than that of Bi, O, and I because of the lower content of La and Au in the samples. In Figure 1d, the O 1s peak is divided into two peaks at 529.9 and 531.5 eV for BOI and 2% A-BOI samples. The first peak located at 529.9 eV is associated with the lattice oxygen, and the second peak centered at 531.5 eV can be assigned to the surface-adsorbed oxygen.[4,33] An additional third peak appeared in the XPS spectra of 2%L-BOI and 2%A−6%L-BOI samples, which can be attributed to the introduction of defective oxygen by La doping. In Figure 1e, the peaks at 834.2 and 851.4 eV of the 6%L-BOI and 2%A−6% L-BOI samples can be assigned to La $3d_{5/2}$ and La $3d_{3/2}$, respectively. The satellite peaks of La $3d_{5/2}$ and La $3d_{3/2}$ can be observed at 838.3 and 855.3 eV, respectively, confirming that La was successfully doped as La^{3+} in the BOI lattice.[34] As shown in Figure 1f, the peaks centered at 83.78 and 87.38 eV are ascribed to Au $4f_{7/2}$ and Au $4f_{5/2}$, respectively, which is in good consistency with the previous report.[35] This indicates that Au nanoparticles were also successfully loaded on the surface of 6%L-BOI sample. As shown in Figure S1a, the peaks at 158.9 and 164.3 eV correspond to Bi $4f_{7/2}$ and Bi $4f_{5/2}$, suggesting that Bi in the L-BOI existed as Bi^{3+}.[8,9] The peaks of I 3d (Figure S1b) located at 619.10 and 630.5 eV correspond to I $3d_{5/2}$ and I $3d_{3/2}$,[8] respectively. Hence, La^{3+} was successfully introduced into the lattice of BOI along with loading of Au nanoparticles.

Figure 2a shows the UV−vis absorption spectra of the as-synthesized BOI, L-BOI, 2%A-BOI and 2%A−6%L-BOI photocatalysts. It can be seen that the pure BOI can only absorb light with wavelengths less than 416 nm. Compared with the pure BOI, La-doped BOI samples exhibited an obviously red shift with the increasing La^{3+} content, indicating that the light response of the samples was markedly enhanced with the increasing La^{3+} content. In addition, a strong absorption peak was observed at 530 nm in the Au-loaded samples, which is related to the SPR effect of Au nanoparticles deposited on the surface of BOI and 6%L-BOI samples.[35] The color of the BOI, 6%L-BOI and 2%A−6%L-BOI samples are white, yellow, and lavender (inset in Figure 2b), respectively. Furthermore, the optical band gaps of pure BOI, 2, 4, 6, and 8% La-doped BOI samples are 2.90, 2.65, 2.43, 2.36, and 2.30

eV, respectively, which were estimated by the equation in previous reported.[8,9]

It is known that lanthanide ions doped in semiconductors can form impurity energy levels to narrow the band gap of semiconductors and improve light absorption.[15,17] To confirm the change in the internal band structure of BOI by introducing La^{3+}, the valence band (VB) positions of the pure BOI and L-BOI samples were measured by XPS-VB analysis. As shown in Figure 2c, the VB positions of the pure BOI and 2, 4, 6, and 8% La-doped BOI samples are 1.77, 1.73, 1.72, 1.65, and 1.60 eV, respectively. Based on the band gaps in Figure 2b and the VB position in Figure 2c, the CBs of pure BOI and 2, 4, 6, and 8% La-doped BOI samples are estimated to be −1.13, −0.92, −0.71, −0.71 and −0.70 eV (Figure 2d), respectively. Therefore, the band gap of the BOI sample was effectively reduced after La^{3+} doping.

The existence of oxygen vacancy in the BOI and La-doped BOI samples was confirmed by EPR spectroscopy (Figure 2e) also. The pure BOI sample shows a very weak EPR signal at $g = 2.003$, whereas La-doped BOI samples show more intense symmetric signal. Such a significant signal is associated with oxygen vacancies, and its intensity is positively correlated with the amount of oxygen vacancy.[4,16] Evidently, the counts of oxygen vacancy in the prepared samples was gradually increased with the increasing La^{3+} content.

N_2 adsorption−desorption isotherms of the pure BOI, 2%A-BOI, 6%L-BOI, and 2%A−6%L-BOI samples are shown in Figure 2f. The Brunauer−Emmett−Teller (BET) specific surface areas of the pure BOI, 2%A-BOI, 6%L-BOI, and 2% A−6%L-BOI samples are 17.11, 18.22, 17.54, and 20.75 $m^2 \cdot g^{-1}$, respectively. Clearly, the BET specific surface areas were increased after loading Au nanoparticles on the surfaces of BOI and 6%L-BOI. The high specific surface area means more active sites on the surface of 2%A−6%L-BOI sample, which is beneficial for the photocatalytic activity of NO removal.

To elucidate the influence of La^{3+} doping on the band structure of BOI, the electronic structures of the BOI and L-BOI were computed by the density functional theory (DFT) method. To further illustrate the effect of oxygen defects, the calculations were run for La-doped BOI in the condition of oxygen defects. The crystal structures, band structures, and partial/total density of states (PDOS/TDOS) of pure BOI, La-doped BOI, and La-doped BOI with oxygen defects are shown in Figures S2 and 3. It can be seen from Figure 3a that the pure BOI is an indirect band gap semiconductor, where the top of VB is located between G and R points and the bottom of the CB is at G point of the Brillouin zone. This indirect transition is beneficial to improve the photocatalytic activity, which is mainly because the excited electrons must move to a certain k-space distance to be migrated to the CB. This reduces the recombination rate of photo-excited charge carriers. Here, the calculated band gap is found to be 2.75 eV, which is smaller than the experimental value (2.90 eV). The underestimation of the band gap is due to the well-known limitation of the generalized gradient approximation.[36] From the band structures shown in Figure 3c,e, the calculated band gap values are about 2.48 and 2.39 eV for La-doped BOI and La-doped BOI with oxygen defects, respectively. The VB top and CB bottom move toward the lower energy levels, which indicate that the oxidation capacity of La-doped BOI could be obviously improved. The narrowed band gap of L-BOI which caused by introducing oxygen vacancies is well consistent with the experimental results. Interestingly, by the virtues of La^{3+} doping and introducing the oxygen defects, the degeneracy of energy levels is reduced due to the decrease of crystal symmetry, leading to the split of energy levels and the generation of the impurity level at the top of VB. The narrowed band gap significantly reduces the transition energy and improves the electronic excitation and transition process, which is favorable for the separation of photo-excited charge carriers. Especially the formed impurity level becomes a capturing center for photo-excited electrons, providing active sites for the oxygen reduction reaction. In addition, the calculated results indicate that the flat bands are formed at the top of VB, supporting the trapping of photo-excited holes. In addition, these flat bands significantly enhance the mobility of charge carriers. The above results indicate that the separation efficiency of electrons and holes could be enhanced and the photocatalytic activity could be obviously improved.

To explore the contribution of different atoms (Bi, O, I, and La) toward the formation of the VB and CB, the PDOS and TDOS were also calculated. For pure BOI (Figure 3b), the top of VB (in the range of −5 to 0 eV) mainly consisted of the O 2p and I 5p orbitals and partially Bi 6s and Bi 6p orbitals, whereas the bottom of CB mainly consisted of Bi 6p and I 5s orbitals. This leads to an indirect electronic transition from O 2p and I 5p states in VB to Bi 6p and I 5s states in CB under light irradiation. For La-doped BOI (Figure 3d), the top of VB (in the range of −5 to 0 eV) is mainly occupied by Bi 6p, O 2p, and I 5p orbitals and has partial contributions from the La 5p and 5d orbitals, whereas the bottom of CB is dominated by Bi 6p, I 5s, and La 5d orbitals. For La-doped BOI with oxygen defects (Figure 3f), the top of VB (in the range of −5 to 0 eV) is basically composed of Bi 6p, O 2p, and I 5p orbitals and partial La 5p and 5d orbitals, whereas the bottom of CB is dominated by Bi 6p, I 5s, and La 5d orbitals. In particular, the defect state is found in the forbidden band because of the existence of the oxygen vacancies, which is well with the results obtained by XPS and UV−vis. Accordingly, the electrons in the VB of La-doped BOI with oxygen defects can be easily excited because of their flat bands and weak hybridization of O and Bi atoms at the top of VB.

Figure S3 shows the SEM images of pure BOI, 2%A-BOI, 6%L-BOI, and 2%A−6%L-BOI samples. It can be seen that the pure BOI photocatalyst possesses spherical microstructures with an average diameter of approximately 2−4 μm, which is constructed by nanosheets with 5−10 nm thickness. Despite the introduction of La^{3+} into the BOI lattice and the deposition of Au nanoparticles on the surface of BOI, all of the samples maintained their spherical structure. The TEM and high-resolution transmission electron microscopy images of the 2% A−6%L/BOI are shown in Figure 4. The well-defined porous microsphere has a diameter of about 3 μm (Figure 4a). Figure 4b,c confirms that Au nanoparticles were successfully loaded on the surface of the microsphere. The HRTEM image of 2% A−6%L/BOI shows in Figure 4d that the spacing of lattice fringes is about 0.24 nm, which is consistent with the (111) plane of Au nanoparticles. In Figure 4e, the spacing of lattice fringes is about 0.271 nm, corresponding to the (204) crystallographic plane of monoclinic Bi_5O_7I. To further elucidate the existence of La element and Au nanoparticles in BOI, the 2%A−6%L/BOI was investigated by EDS mapping. In Figure S4, it is evident that the Bi, O, and I elements are evenly distributed in the microspheres. Figure 4f,g shows that La is also distributed evenly in the whole microspheres, whereas Au nanoparticles have a uniform

DOI: 10.1021/acsami.9b14300
ACS Appl. Mater. Interfaces 2019, 11, 37822−37832

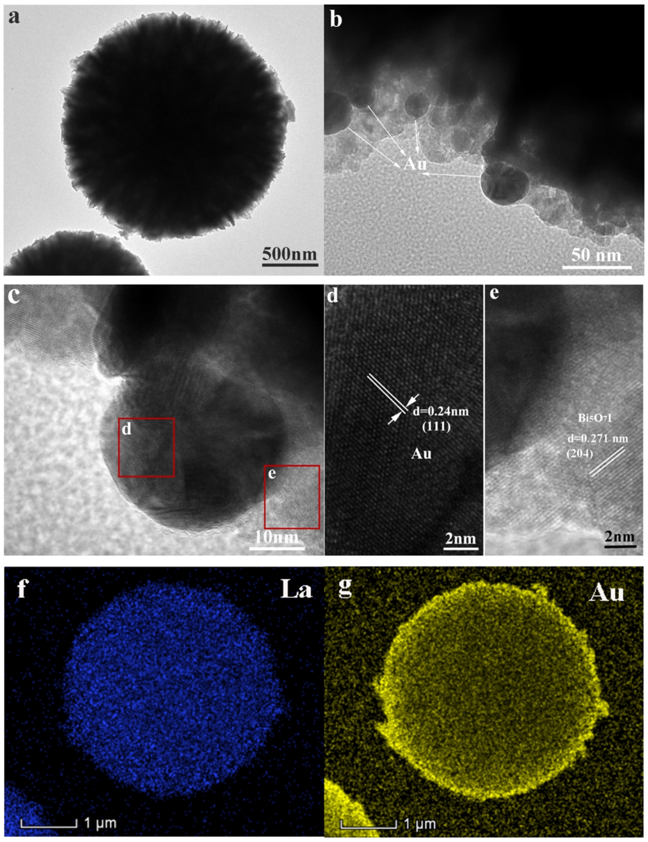

Figure 4. TEM (a,b), HRTEM (c–e) images, and EDS element mapping images of La (f) and Au (g) of the 2%A–6%L-BOI.

distribution on the surface of L-BOI microspheres. This distribution indicates that La^{3+} was successfully doped into the BOI lattice and Au nanoparticles were finely loaded on the surface of L-BOI microspheres.

3.2. Photocatalytic Activity. Figure 5a shows the photocatalytic NO removal performance of the pure BOI, L-BOI, 2%A-BOI and 2%A–6%L-BOI samples. As shown in Figure 5a, pure BOI exhibited a poor photocatalytic performance (20.4% of NO removal rate) due to its poor visible-light absorption (E_g = 2.9 eV). Obviously, L-BOI samples showed a remarkably improved photocatalytic performance for NO removal (Figure 5b). Among the L-BOI samples, 6%L-BOI exhibited the highest photocatalytic activity (42.7% of NO removal rate). The enhanced performance of the L-BOI samples is mainly attributed to their narrowed band gap and inhibition of the recombination of photo-excited electron–hole pairs. It is well known that La^{3+} can capture photo-induced electrons to improved separation efficiency. However, when the La^{3+} content reached to 8 mol %, the photocatalytic activity began to decline due to the formation of the recombination center with excess La^{3+}. Figure 5c shows that the photocatalytic NO removal rates of BOI, 2%A-BOI, 6%L-BOI, and 2%A–6%L-BOI samples are 20.4, 34.2, 42.7, and 54.5%, respectively. It can be seen that 2%A-BOI and 2%A–6%L-BOI also showed a remarkable enhancement performance as compared to the BOI sample. This indicates that the Au nanoparticles loaded on the surface of BOI (or 6%L-BOI) could enhance the photocatalytic activity owing to the SPR effect.[35] Furthermore, Au nanoparticles can trap photo-generated electrons by the Schottky barrier to inhibit the recombination of photo-induced carries.[37] During the removal process, the generation of toxic NO_2 intermediate was also monitored (Figure 5d). The concentration of NO_2 in the presence of BOI, 2%A-BOI, 6%L-BOI, and 2%A–6%L-BOI samples was about 12, 11, 10, and 5 ppb, respectively. It is believed that the generation of NO_2 during the photocatalytic process is related to the number of active species and the oxidative activity of radical species. The present oxygen vacancies introduced by La doping can increase the number of active species and enhance the oxidative activity of radical species, promoting the complete oxidation ability for NO. Moreover, the deposition of Au nanoparticles on BOI could also lead to a decrease yield of NO_2. To evaluate the photocatalytic stability of the 6%La-BOI and 2%A–6%L-BOI, five successive photocatalytic cycles were carried out, and the results are given in Figure 5e. The results indicate that the NO removal rate over the 2%A–6%L-BOI sample still maintained high performance after five cycles, indicating the outstanding stability and cycleability. In Figure 5f, the XRD patterns of the 2%A–6%L-BOI sample before and after the photocatalytic reaction are nearly identical, indicating the stability of the crystal structure.

3.3. Mechanism. The surface photovoltage spectroscopy (SPS) was applied to study the separation and transfer behaviors of photo-induced charge carriers under the monochromic excitation. A stronger SPS signal means a higher separation efficiency of photo-excited charge carriers. The pure BOI, 2%A-BOI, 6%L-BOI and 2%A–6%L-BOI samples show a clearly positive SPS signal after 300–450 nm stimulated light (Figure 6a). In the SPS measurement process, the disappearance of SPS signal less than 300 nm can be attributed to the indium tin oxide glass where it commendably absorbed the light with the wavelengths less than 300 nm. As an n-type semiconductor, the surface band bends of BOI upward in the air, indicating that the orientation of the internal electric field is from inside to the outside.[38] Thus, the photo-induced holes are easily transferred to the surface of the semiconductor, whereas the photo-induced electrons are readily moved to the inside of semiconductor. With the introduction of La^{3+} into BOI, the surface barrier is increased, and the space of charge region is compressed. Therefore, the photo-induced electron–hole pairs are efficiently separated by a large electric field. In addition, in the Au–BOI composites, the Schottky barrier at the interface between Au and BOI is formed due to the Fermi level of BOI higher than that of Au.[39] The Schottky barrier can effectively capture electrons and transfer to the surface, suppressing the recombination of electron–hole pairs and enhancing the signal of SPS.[40] Therefore, the 2%A–6%L-BOI sample shows a higher SPS signal than pure BOI, 2%A-BOI, and 6%L-BOI.

Photoluminescence (PL) spectroscopy was used to further characterize the recombination of photo-excited e^-/h^+ pairs of the prepared samples. The PL spectra of pure BOI, 2%A-BOI, 6%L-BOI, and 2%A–6%L-BOI samples were measured with 325 nm excitation wavelength (Figure S5). It is clear that the intensity of the PL spectrum of 2%A–6%L-BOI is much lower than that of other samples. The intensity of the PL spectra of 6%L/BOI and 2%A-BOI are also lower than that of pure BOI, indicating that the La^{3+} doping and deposition of Au nanoparticles improve significantly the separation and transfer efficiency of photo-excited carriers.[41,42] This is well consistent with the experimental results of photocatalytic NO removal under visible-light irradiation.

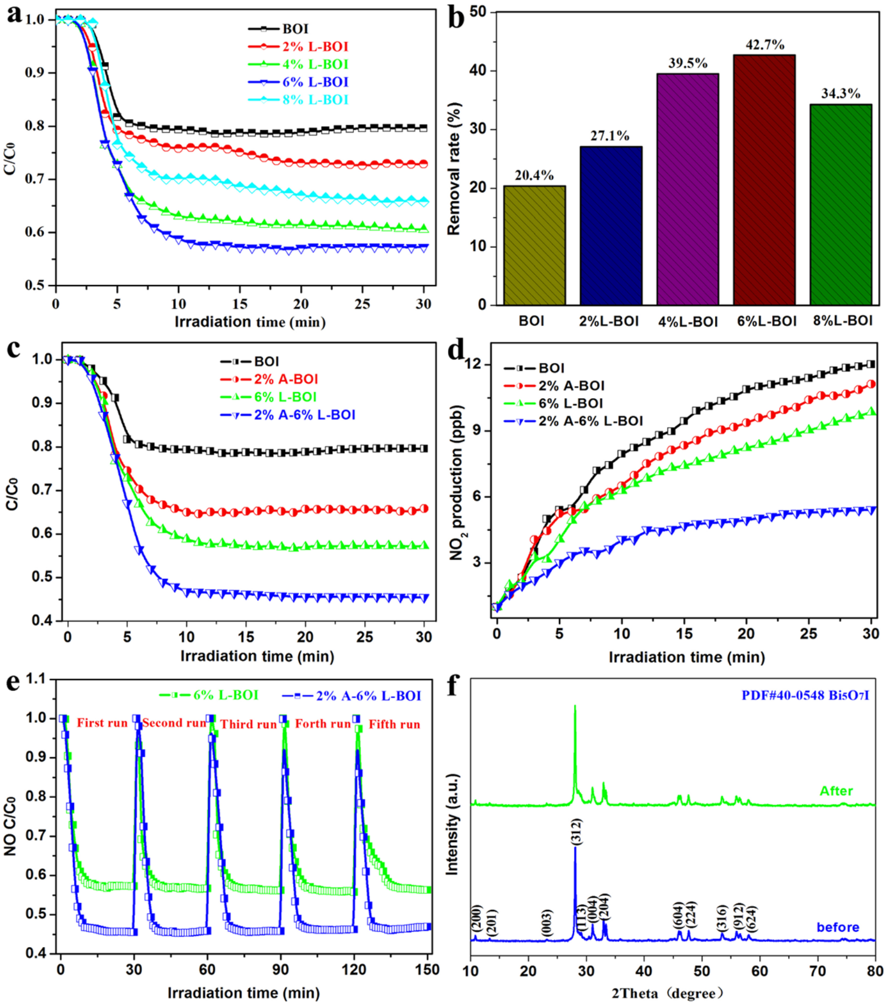

Figure 5. Photocatalytic NO removal efficiency (a,b) of BOI and La-doped BOI samples under visible-light irradiation; photocatalytic NO removal efficiency (c) and the variation of NO_2 concentration (d) by BOI, 2%A-BOI, 6%L-BOI, and 2%A−6%L-BOI samples; photocatalytic NO removal efficiency by 6%L/BOI and 2%A−6%L-BOI samples for five cycles (e); XRD patterns of 2%A−6% La/BOI before and after the photocatalytic reaction (f).

In order to propose the reaction mechanism for the photocatalytic NO removal over the 2%A−6%L-BOI sample, the scavenger tests were executed to investigate the type of active species. As shown in Figure 6b, after the addition of IPA, the removal rate did not significantly change compared with the sample obtained without adding scavengers. It indicates that $^\bullet OH$ has a nonsignificant role during the photocatalytic removal process. However, the removal rate of NO was reduced after the addition of KI and BQ, confirming that both h^+ and $^\bullet O_2^-$ played an important role during the NO removal process. It is noteworthy that the addition of $K_2Cr_2O_7$ in the reaction system decreased the NO removal efficiency significantly, indicating that the photogenerated electrons had a significant role in the whole process of NO photocatalytic removal.

To further distinguish the presence of active species with the 2%A−6%L-BOI photocatalyst during the photocatalytic reaction process, ESR spectroscopic measurements were conducted by 5,5-dimethyl-1-pyrroline N-oxide (DMPO) spin-trapping adducts to detect the $^\bullet O_2^-$ and $^\bullet OH$ radical species. As shown in Figure 6c,d, no signal could be detected without light irradiation. However, a series of strong characteristic peaks of DMPO-$^\bullet O_2^-$ were evidently detected after visible-light irradiation, implying that the sample can produce massive $^\bullet O_2^-$ radical species (Figure 6c). Furthermore, no signal representing $^\bullet OH$ radical species was observed over the 2%A−6%L-BOI sample even after irradiation for 12 min (Figure 6d). The trapping experiments and ESR results confirm that h^+, e^-, and $^\bullet O_2^-$ radical species played an important role during the NO removal process.

Furthermore, in situ DRIFTS with the reaction gas was used to study the byproducts generated during the processes of adsorption in the dark and photocatalysis process on the surface of 2%A−6%L-BOI, respectively. The obtained FTIR results are used to investigate the NO removal mechanism. First, in the dark condition, several intermediates were detected over the 2%A−6%L-BOI surface. As shown in Figure 7a, the bands are observed at 808, 914, 1035, 1193, 1400, 1619, and 2360 cm^{-1}.[43,44] The bands at 914 and 1619 cm^{-1} can correspond to the NO bands. It is worth noting that the intensity of these bands becomes higher with the passage of time because of the increase in adsorption of NO molecules on the sample surface. The mixed gas (O_2 and NO) was co-adsorbed on the surface of the sample, and NO was then oxidized to N_2O_2 and NO_2 by O_2 directly. Thus, the bands at 1035 cm^{-1} (N_2O_2) and 808 cm^{-1} (NO_2) were detected. In

DOI: 10.1021/acsami.9b14300
ACS Appl. Mater. Interfaces 2019, 11, 37822−37832

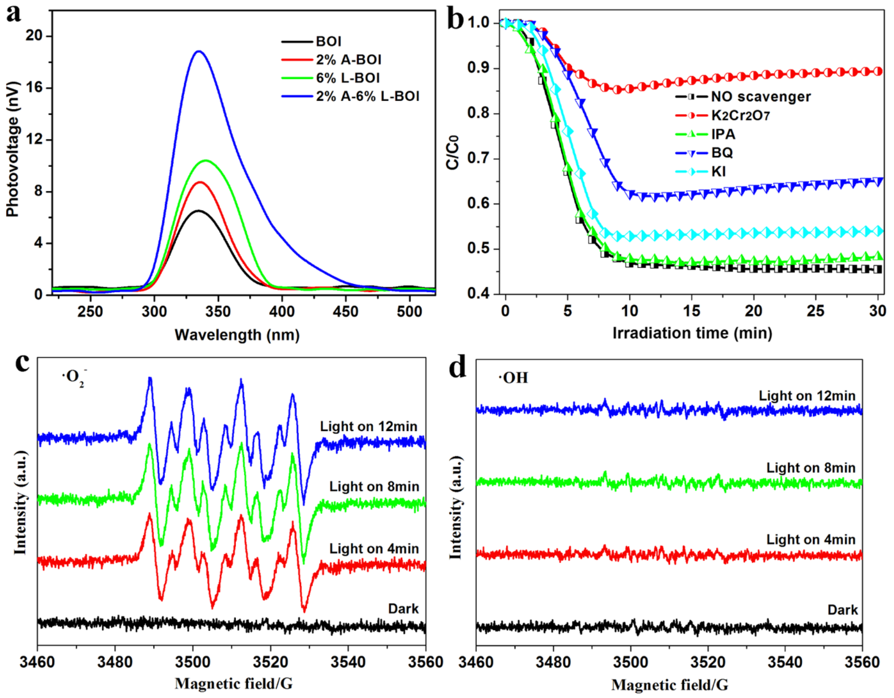

Figure 6. (a) SPS spectra of pure BOI, 2%A-BOI, 6%L-BOI, and 2%A–6%L-BOI samples; (b) photocatalytic activity for the photo-oxidative removal of NO of 2%A–6%L-BOI in the presence of various scavengers; ESR spectra of DMPO-$^{\bullet}O_2^-$ (c) and DMPO-$^{\bullet}$OH (d) over 2%A–6%L-BOI photocatalyst in dark and under light irradiation.

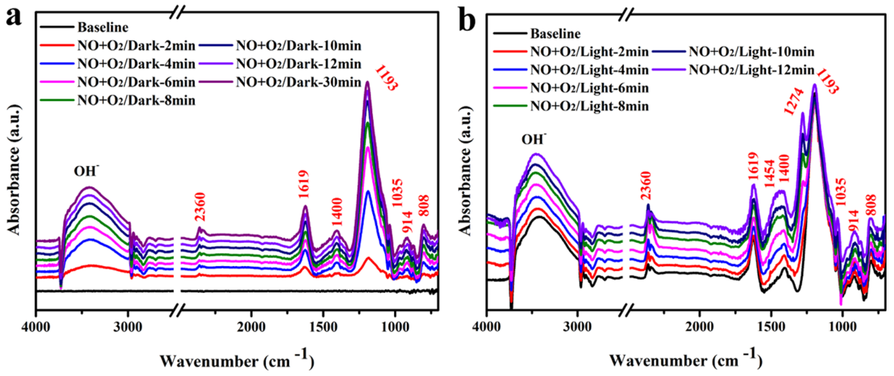

Figure 7. In situ FTIR spectra of adsorption in the dark (a) and photocatalysis process under visible-light irradiation (b) on the surface of 2%A–6%L-BOI.

addition, the bands representing NO_2^+ (1400 cm^{-1}) and bidentate nitrites (NO_3^-) (1193 cm^{-1}) appeared.[45,46] The results suggest that NO_x gas, including NO, NO_2, and N_2O_2, was further oxidized by oxidizing species. This phenomenon can be ascribed to the O_2 on the sample surface, accepting the free electrons located around the oxygen defects in the sample surface to form $^{\bullet}O_2^-$ species.[47] Consequently, the partial NO was oxidized to the final products (NO_2^+ or NO_3^-) in the dark. Besides, the NO can react with surface-adsorbed water molecules to form NO_2^+ and OH^-; therefore, the bands at 2360 and 3500 cm^{-1} can be observed.[43] Based on the in situ DRIFTS results, here we propose the possible reaction processes in the dark condition as shown in eqs S1–S4 in the Supporting Information.

During the photocatalytic reaction under light irradiation, the intensity of bands observed in the dark was changed along with the emergence of new bands for NO_3^- (1274 cm^{-1}) and NO_2^- (1545 cm^{-1}), as shown in Figure 7b. Under visible-light irradiation, the e^-/h^+ pairs were generated, and photogenerated e^- (eq S5 in the Supporting Information) reacted with adsorbed O_2 to produce $^{\bullet}O_2^-$ radicals (eqs S6–S8 in the Supporting Information).[44,45,47] The h^+, e^-, and $^{\bullet}O_2^-$ radicals are able to further oxidize NO_x and NO_2^+ generated in the dark process to prevent the further increase of toxic intermediates (eqs S8–S12 in the Supporting Information).[48] Therefore, it is observed that the intensity of bands belonging to nitrate and nitrite became stronger, and the bands assignable to NO_x (including N_2O_2 and NO_2) were reduced when the light was turned on. These observations are in accordance to the presence of oxygen vacancies and Au nanoparticles in the 2%A–6%L-BOI composites, resulting in the production of massive free radicals and enhancing the oxidative activity of radical species.

Furthermore, the Fermi level of the compounds can be obtained via CASTEP codes. As shown in Figure 8, the positions of the Fermi levels of BOI and L-BOI are located at

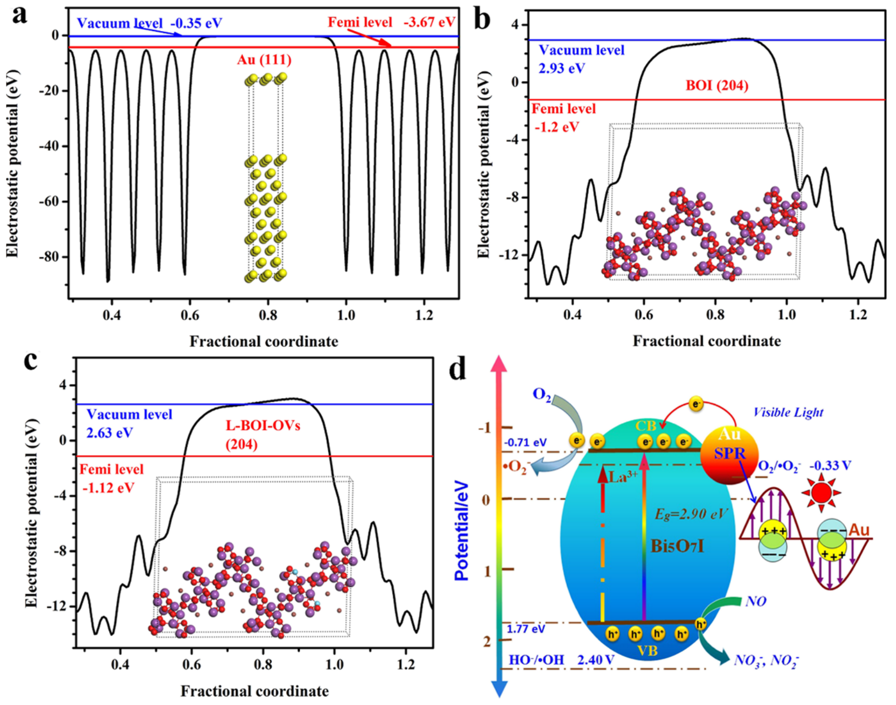

Figure 8. Crystal structures and work functions of (a) Au(111), (b) BOI (204), and (c) L-BOI-OVs (204); (d) proposed mechanism for the photo-oxidative removal of NO by 2%A−6%L-BOI under visible-light irradiation.

−1.2 and −1.12 eV/AVS, respectively. The position of the Fermi level of Au is located at −0.367 eV/AVS, suggesting that the Fermi level of Au is lower than that of BOI. According to the positions of the Fermi levels and XPS-VB results, the VB edges of BOI and L-BOI are positioned at −2.97 and −2.77 eV/AVS, respectively. In addition, based on the UV−vis absorption spectra, the band gaps of BOI and 6%L-BOI are 2.9 and 2.36 eV, respectively. Thus, the CB edges of BOI and L-BOI are located at −0.07 and −0.41 eV/AVS, respectively. Moreover, the origin of charge transfer at the interface can be revealed by work function analysis. Therefore, the work functions of Au, BOI, and L-BOI are also calculated based on the experimental results in Figure 8. The work functions of Au, BOI, and L-BOI are determined to be 3.54 (Figure 8a), 5.85 (Figure 8b), and 5.69 eV (Figure 8c). The order of the work function is Au < L-BOI < BOI, and the photogenerated electrons in Au nanoparticles will be available to be transferred to L-BOI than to BOI. The Fermi level of Au is upward, whereas the Fermi levels of BOI and L-BOI are downward until the equilibrium is obtained under the circumstances. Hence, the transfer of electrons can inhibit the recombination of photogenerated charge carriers.

According to the above results and discussion, a possible photocatalytic mechanism for NO removal by 2%A−6%L-BOI composites photocatalyst is proposed as shown in Figure 8d. When La^{3+} is introduced into the BOI lattice, the band gap decreases from 2.90 to 2.36 eV because of the formation of a doping level and oxygen vacancy below the CB of BOI.[8,45] Therefore, under visible-light irradiation, the formation of photo-excited e^- and h^+ takes place between the doping levels of La^{3+} and the VB of BOI. The h^+ can directly oxidize NO to form NO_3^-. The photo-excited e^- react with adsorbed O_2 to generate $^{\bullet}O_2^-$ that reacts with NO to form NO_3^-.[43] In addition, Au nanoparticles loaded on the surface of L-BOI inhibit the recombination of photo-excited charge carriers, as well as the light response is also enhanced utilizing the SPR effect of Au nanoparticles. Thus, the photocatalytic performance of the prepared 2%A−6%L-BOI composite photocatalyst was significantly improved.

4. CONCLUSIONS

Au nanoparticle-loaded La-doped Bi_5O_7I microspheres (2%A−6%L-BOI) were prepared successfully. Both L-BOI and 2% Au−6%L-BOI photocatalysts showed a stronger visible-light absorption as compared to the pure BOI. The 2%A−6%L-BOI photocatalyst exhibited an obvious improved visible-light photocatalytic performance for the NO removal compared with pure BOI, L-BOI, and A-BOI photocatalysts. It was found that the 2%A−6%L-BOI photocatalyst also could reduce the concentration of NO_2 formed as the intermediate. The photocatalytic performance improvement of the 2%A−6%L-BOI is ascribed to the synergistic effect of La ions doping, oxygen vacancy, and plasmonic effect of Au nanoparticles. According to trapping tests and ESR measurements, h^+, e^-, and $^{\bullet}O_2^-$ were involved in the photocatalytic NO removal process. The as-prepared photocatalyst showed excellent photostability and repeatability and would be used as a promising material in the air purification applications.

■ ASSOCIATED CONTENT

Ⓢ Supporting Information

The Supporting Information is available free of charge on the ACS Publications website at DOI: 10.1021/acsami.9b14300.

Synthesis process of BiOI microspheres; characterization for samples; SPS measurement process; photocatalytic NO removal process; in situ FTIR studies of photo-oxidative removal of NO; trapping experiments; DFT calculations; high-resolution XPS spectra of Bi 4f and I 3d; calculated models of pure Bi_5O_7I, La-doped Bi_5O_7I and La-doped Bi_5O_7I with oxygen defects; SEM images of the pure BOI, 2%A-BOI, 6%L-BOI, and 2%A−6%L-BOI; EDS element mapping images of 2%A−6%L-BOI; PL spectra of the pure BOI, 6%-L-BOI, 2%-A-BOI, and 2%A−6%-L-BOI samples; and possible reaction equations in dark and under visible-light irradiation (PDF)

AUTHOR INFORMATION

Corresponding Authors

*E-mail: zgq2006@snnu.edu.cn. Phone/Fax: +86-29-81530750 (G.Z.).
*E-mail: huangyu@ieecas.cn (Y.H.).

ORCID

Gangqiang Zhu: 0000-0001-5708-9446
Qadeer-Ul Hassan: 0000-0002-2317-9758
Yu Huang: 0000-0003-3334-4849
Mirabbos Hojamberdiev: 0000-0002-5233-2563

Notes

The authors declare no competing financial interest.

ACKNOWLEDGMENTS

This work was supported by the National Natural Science Foundation of China (grant no. 51772183), the Key Research and Development Program of Shaanxi Province (grant no. 2018ZDCXL-SF-02-04), and the Fundamental Research Funds for the Central Universities (grant nos. GK201903023 and GK201801005). M.H. would like to thank the Alexander von Humboldt (AvH) Stiftung for the research award.

REFERENCES

(1) Chang, L.; Zhu, G.; Hassan, Q.-U.; Cao, B.; Li, S.; Jia, Y.; Gao, J.; Zhang, F.; Wang, Q. Synergetic Effects of Pd^0 Metal Nanoparticles and Pd^{2+} Ions on Enhanced Photocatalytic of $ZnWO_4$ Nanorods for Nitric Oxide Removal. *Langmuir* **2019**, *35*, 11265−11274.

(2) Shi, X.; Wang, P.; Li, W.; Bai, Y.; Xie, H.; Zhou, Y.; Ye, L. Change in Photocatalytic NO Removal Mechanisms of Ultrathin BiOBr/BiOI via NO_3^- Adsorption. *Appl. Catal., B* **2019**, *243*, 322−329.

(3) Huo, W. C.; Dong, X.; Li, J. Y.; Liu, M.; Liu, X. Y.; Zhang, Y. X.; Dong, F. Synthesis of Bi_2WO_6 with Gradient Oxygen Vacancies for Highly Photocatalytic NO Oxidation and Mechanism Study. *Chem. Eng. J.* **2019**, *361*, 129−138.

(4) Rao, F.; Zhu, G.; Hojamberdiev, M.; Zhang, W.; Li, S.; Gao, J.; Zhang, F.; Huang, Y.; Huang, Y. Uniform Zn^{2+}-Doped BiOI Microspheres Assembled by Ultrathin Nanosheets with Tunable Oxygen Vacancies for Super-Stable Removal of NO. *J. Phys. Chem. C* **2019**, *123*, 16268−16280.

(5) She, H.; Sun, Y.; Li, S.; Huang, J.; Wang, L.; Zhu, G.; Wang, Q. Synthesis of Non-noble Metal Nickel Doped Sulfide Solid Solution for Improved Photocatalytic Performance. *Appl. Catal., B* **2019**, *245*, 439−447.

(6) Yu, H.; Li, J.; Zhang, Y.; Yang, S.; Han, K.; Dong, F.; Ma, T.; Huang, H. Three-in-One Oxygen Vacancies: Whole Visible-Spectrum Absorption, Efficient Charge Separation, and Surface Site Activation for Robust CO_2 Photoreduction. *Angew. Chem., Int. Ed.* **2019**, *58*, 3880−3884.

(7) Wang, Z.; Huang, Y.; Ho, W.; Cao, J.; Shen, Z.; Lee, S. C. Fabrication of $Bi_2O_2CO_3$/g-C_3N_4 Heterojunctions for Efficiently Photocatalytic NO in Air Removal: In-situ Self-sacrificial Synthesis, Characterizations and Mechanistic Study. *Appl. Catal., B* **2016**, *199*, 123−133.

(8) Liu, Y.; Zhu, G.; Gao, J.; Zhu, R.; Hojamberdiev, M.; Wang, C.; Wei, X.; Liu, P. Novel Synergy of Er^{3+}/Fe^{3+} co-doped Porous BOI Microspheres with Enhanced Photocatalytic Activity under Visible-light Irradiation. *Appl. Catal., B* **2017**, *205*, 421−432.

(9) Zhu, G.; Li, S.; Gao, J.; Zhang, F.; Liu, C.; Wang, Q.; Hojamberdiev, M. Constructing a 2D/2D $Bi_2O_2CO_3$/$Bi_4O_5Br_2$ Heterostructure as a Direct Z-Scheme Photocatalyst with Enhanced Photocatalytic Activity for NO_x Removal. *Appl. Surf. Sci.* **2019**, *493*, 913−925.

(10) Liu, R.; Li, H.; Duan, L.; Shen, H.; Zhang, Y.; Zhao, X. In Situ Synthesis and Enhanced Visible Light Photocatalytic Activity of C-TiO_2 Microspheres/Carbon Quantum Dots. *Ceram. Int.* **2017**, *43*, 8648−8654.

(11) Chen, H.; Nanayakkara, C. E.; Grassian, V. H. Titanium Dioxide Photocatalysis in Atmospheric Chemistry. *Chem. Rev.* **2012**, *112*, 5919−5948.

(12) Rauf, M. A.; Meetani, M. A.; Hisaindee, S. An Overview on the Photocatalytic Degradation of Azo Dyes in the Presence of TiO_2 Doped with Selective Transition Metals. *Desalination* **2011**, *276*, 13−27.

(13) Jayachandraiah, C.; Siva Kumar, K.; Krishnaiah, G.; Madhusudhana Rao, N. Influence of Dy Dopant on Structural and Photoluminescence of Dy-doped ZnO Nanoparticles. *J. Alloys Compd.* **2015**, *623*, 248−254.

(14) Obregón, S.; Colón, G. Heterostructured Er^{3+} Doped $BiVO_4$ with Exceptional Photocatalytic Performance by Cooperative Electronic and Luminescence Sensitization Mechanism. *Appl. Catal., B* **2014**, *158−159*, 242−249.

(15) Yang, J.; Liang, Y.; Li, K.; Yang, G.; Zhu, Y.; Liu, S.; Lei, W. New Reaction Pathway Induced by the Synergistic Effects of Bi Plasmon and La^{3+} Doping for Efficient Visible Light Photocatalytic Reaction on BiOCl. *Appl. Surf. Sci.* **2018**, *458*, 769−780.

(16) Liu, D.; Wu, Z.; Tian, F.; Ye, B.-C.; Tong, Y. Synthesis of N and La Co-doped TiO_2/AC Photocatalyst by Microwave Irradiation for the Photocatalytic Degradation of Naphthalene. *J. Alloys Compd.* **2016**, *676*, 489−498.

(17) Villa, K.; Murcia-López, S.; Morante, J. R.; Andreu, T. An Insight on the Role of La in Mesoporous WO_3 for the Photocatalytic Conversion of Methane into Methanol. *Appl. Catal., B* **2016**, *187*, 30−36.

(18) Rahman, A.; Jayaganthan, R. Synthesis, Characterization and Photocatalytic Studies of La, Dy-doped ZnO Nanoparticles. *Trans. Indian Inst. Met.* **2017**, *70*, 1063−1074.

(19) Yotburut, B.; Thongbai, P.; Yamwong, T.; Maensiri, S. Electrical and Nonlinear Current-Voltage Characteristics of La-Doped $BiFeO_3$ Ceramics. *Ceram. Int.* **2017**, *43*, 5616−5627.

(20) Han, J.; Zhu, G.; Hojamberdiev, M.; Peng, J.; Zhang, X.; Liu, Y.; Ge, B.; Liu, P. Rapid Adsorption and Ahotocatalytic Activity for Rhodamine B and Cr(VI) by Ultrathin BiOI Nanosheets with Highly Exposed {001} Facets. *New J. Chem.* **2015**, *39*, 1874−1882.

(21) Huang, H.; Xiao, K.; Zhang, T.; Dong, F.; Zhang, Y. Rational Design on 3D Hierarchical Bismuth Oxyiodides via in Situ Self-Template Phase Transformation and Phase-junction Construction for Optimizing Photocatalysis against Diverse Contaminants. *Appl. Catal., B* **2017**, *203*, 879−888.

(22) Liu, H.; Su, Y.; Chen, Z.; Jin, Z.; Wang, Y. $Bi_7O_9I_3$/Reduced Graphene Oxide Composite as an Efficient Visible-Light-Driven Photocatalyst for Degradation of Organic Contaminants. *J. Mol. Catal. A: Chem.* **2014**, *391*, 175−182.

(23) Cheng, H.; Huang, B.; Dai, Y. Engineering BiOX (X = Cl, Br, I) Nanostructures for Highly Efficient Photocatalytic Applications. *Nanoscale* **2014**, *6*, 2009−2026.

(24) Zhang, K.; Liu, C.; Huang, F.; Zheng, C.; Wang, W. Study of the Electronic Structure and Photocatalytic Activity of the BiOCl Photocatalyst. *Appl. Catal., B* **2006**, *68*, 125−129.

(25) Li, M.; Yu, S.; Huang, H.; Li, X.; Feng, Y.; Wang, C.; Wang, Y.; Ma, T.; Guo, L.; Zhang, Y. , Y. H. Unprecedented Eighteen-faceted BiOCl with Ternary Facet Junction Boosting Cascade Charge Flow and Photo-redox. *Angew. Chem., Int. Ed.* **2019**, *58*, 9517−9521.

(26) Xia, J.; Ji, M.; Di, J.; Wang, B.; Yin, S.; He, M.; Zhang, Q.; Li, H. Improved Photocatalytic Activity of Few-layer $Bi_4O_5I_2$ Nanosheets Induced by Efficient Charge Separation and Lower Valence Position. *J. Alloys Compd.* **2017**, *695*, 922−930.

DOI: 10.1021/acsami.9b14300

(27) Zhao, Z.; Wang, M.; Yang, T.; Fang, M.; Zhang, L.; Zhu, H.; Tang, C.; Huang, Z. In Situ Co-precipitation for Synthesis of an Ag/AgBr/Bi_5O_7I Heterojunction for Enhanced Visible-Light Photocatalysis. *J. Mol. Catal. A: Chem.* **2016**, *424*, 8−16.

(28) Liu, Q.-C.; Ma, D.-K.; Hu, Y.-Y.; Zeng, Y.-W.; Huang, S.-M. Various Bismuth Oxyiodide Hierarchical Architectures: Alcohothermal-Controlled Synthesis, Photocatalytic Activities, and Adsorption Capabilities for Phosphate in Water. *ACS Appl. Mater. Interfaces* **2013**, *5*, 11927−11934.

(29) Bai, Y.; Ye, L.; Chen, T.; Wang, L.; Shi, X.; Zhang, X.; Chen, D. Facet-Dependent Photocatalytic N_2 Fixation of Bismuth-Rich Bi_5O_7I Nanosheets. *ACS Appl. Mater. Interfaces* **2016**, *8*, 27661−27668.

(30) Han, J.; Zhu, G.; Hojamberdiev, M.; Peng, J.; Liu, P. Temperature Effect on Phase Transition and Morphological Transformation of BiOI Microspheres to Bi_5O_7I Microstructures. *Mater. Lett.* **2016**, *169*, 122−125.

(31) Li, Y.; Song, Z.; Li, C.; Wan, R.; Qiu, J.; Yang, Z.; Yin, Z.; Yang, Y.; Wang, X.; Wang, Q. Efficient Near-infrared to Visible and Ultraviolet Upconversion in Polycrystalline BiOCl: Er^{3+}/Yb^{3+} Synthesized at Low Temperature. *Ceram. Int.* **2013**, *39*, 8911−8916.

(32) Zhang, Q.; Huang, Y.; Peng, S.; Huang, T.; Cao, J.-j.; Ho, W.; Lee, S. Synthesis of $SrFe_xTi_{1-x}O_{3-\delta}$ Nanocubes with Tunable Oxygen Vacancies for Selective and Efficient Photocatalytic NO Oxidation. *Appl. Catal., B* **2018**, *239*, 1−9.

(33) Xu, M.; Han, L.; Dong, S. Facile Fabrication of Highly Efficient g-C_3N_4/Ag_2O Heterostructured Photocatalysts with Enhanced Visible-Light Photocatalytic Activity. *ACS Appl. Mater. Interfaces* **2013**, *5*, 12533−12540.

(34) Yu, Y.; Piao, L.; Xia, J.; Wang, W.; Geng, J.; Chen, H.; Xing, X.; Li, H. A Facile One-pot Synthesis of N-La Co-doped TiO2 Porous Materials with Bio-hierarchical Architectures and Enhanced Photocatalytic Activity. *Mater. Chem. Phys.* **2016**, *182*, 77−85.

(35) Jiang, D.; Wen, B.; Xu, Q.; Gao, M.; Li, D.; Chen, M. Plasmonic Au Nanoparticles/$KCa_2Nb_3O_{10}$ Nanosheets 0D/2D Heterojunctions with Enhanced Photocatalytic Activity Towards the Degradation of Tetracycline Hydrochloride. *J. Alloys Compd.* **2018**, *762*, 38−45.

(36) Perdew, J. P.; Levy, M. Physical Content of the Exact Kohn-Sham Orbital Energies: Band Gaps and Derivative Discontinuities. *Phys. Rev. Lett.* **1983**, *51*, 1884−1887.

(37) Liqiang, J.; Dejun, W.; Baiqi, W.; Shudan, L.; Baifu, X.; Honggang, F.; Jiazhong, S. Effects of Noble Metal Modification on Surface Oxygen Composition, Charge Separation and Photocatalytic Activity of ZnO Nanoparticles. *J. Mol. Catal. A: Chem.* **2006**, *244*, 193−200.

(38) Chen, F.; Huang, H.; Guo, L.; Zhang, Y.; Ma, T. The Role of Polarization in Photocatalysis. *Angew. Chem., Int. Ed.* **2019**, *58*, 10061−10073.

(39) Gupta, A. K.; Hsu, C.-H.; Chen, C.-H.; Purwidyantri, A.; Prabowo, B. A.; Wang, J.-L.; Tian, Y.-C.; Lai, C.-S. Au-spotted Zinc Oxide Nano-hexagonrods Structure for Plasmon Photoluminescence Sensor. *Sens. Actuators, B* **2019**, *290*, 100−109.

(40) Xiong, Y.; Chen, J.; Wiley, B.; Xia, Y.; Yin, Y.; Li, Z.-Y. Size-Dependence of Surface Plasmon Resonance and Oxidation for Pd Nanocubes Synthesized Via a Seed Etching Process. *Nano Lett.* **2005**, *5*, 1237−1242.

(41) Liu, Y.; Zhu, G.; Gao, J.; Hojamberdiev, M.; Zhu, R.; Wei, X.; Guo, Q.; Liu, P. Enhanced Photocatalytic Activity of $Bi_4Ti_3O_{12}$ Nanosheets by Fe^{3+}-Doping and the Addition of Au Nanoparticles: Photodegradation of Phenol and Bisphenol A. *Appl. Catal., B* **2017**, *200*, 72−82.

(42) Zhang, Q.; Huang, Y.; Xu, L.; Cao, J.-j.; Ho, W.; Lee, S. C. Visible-Light-Active Plasmonic Ag-$SrTiO_3$ Nanocomposites for the Degradation of NO in Air with High Selectivity. *ACS Appl. Mater. Interfaces* **2016**, *8*, 4165−4174.

(43) Wu, J.; Cheng, Y. In Situ FTIR Study of Photocatalytic NO Reaction on Photocatalysts under UV Irradiation. *J. Catal.* **2006**, *237*, 393−404.

(44) Papailias, I.; Todorova, N.; Giannakopoulou, T.; Ioannidis, N.; Boukos, N.; Athanasekou, C. P.; Dimotikali, D.; Trapalis, C. Chemical vs Thermal Exfoliation of g-C_3N_4 for NO_x Removal under Visible Light Irradiation. *Appl. Catal., B* **2018**, *239*, 16−26.

(45) Wang, H.; Zhang, W.; Li, X.; Li, J.; Cen, W.; Li, Q.; Dong, F. Highly Enhanced Visible Light Photocatalysis and in Situ FT-IR Studies on Bi Metal Defective BiOCl Hierarchical Microspheres. *Appl. Catal., B* **2018**, *225*, 218−227.

(46) Hadjiivanov, K. I. Identification of Neutral and Charged N_xO_y Surface Species by IR Spectroscopy. *Catal. Rev.* **2000**, *42*, 71−144.

(47) Li, X.; Zhang, W.; Cui, W.; Li, J.; Sun, Y.; Jiang, G.; Huang, H.; Zhang, Y.; Dong, F. Reactant Activation and Photocatalysis Mechanisms on Bi-Metal@Bi_2GeO_5 with Oxygen Vacancies: A Combined Experimental and Theoretical Investigation. *Chem. Eng. J.* **2019**, *370*, 1366−1375.

(48) Li, J.; Zhang, W.; Ran, M.; Sun, Y.; Huang, H.; Dong, F. Synergistic Integration of Bi Metal and Phosphate Defects on Hexagonal and Monoclinic $BiPO_4$: Enhanced Photocatalysis and Reaction Mechanism. *Appl. Catal., B* **2019**, *243*, 313−321.